AGU100 ADVANCING EARTH AND SPACE SCIENCE

JGR Earth Surface

RESEARCH ARTICLE
10.1029/2018JF004802

Basal Stress Equations for Granular Debris Masses on Smooth or Discretized Slopes

Richard M. Iverson[1] and **David L. George**[1]

[1]U.S. Geological Survey, Vancouver, WA, USA

Key Points:
- Newly derived formulas provide good estimates of static shear and normal stresses measured beneath wet granular debris masses on slopes
- Specialized versions of the new formulas apply on horizontal tread surfaces of topography discretized in digital elevation models
- Apparent basal friction acting on horizontal tread surfaces differs predictably from friction acting on smoothly sloping slip surfaces

Correspondence to:
R. M. Iverson,
riverson@usgs.gov

Citation:
Iverson, R. M., & George, D. L. (2019). Basal stress equations for granular debris masses on smooth or discretized slopes. *Journal of Geophysical Research: Earth Surface*, *124*, 1464–1484. https://doi.org/10.1029/2018JF004802

Received 2 JUL 2018
Accepted 30 APR 2019
Accepted article online 7 MAY 2019
Published online 14 JUN 2019

Abstract Knowledge of basal stresses is essential for analyzing slope stability and modeling the dynamics and erosive potential of debris flows and avalanches. Here we derive and test new algebraic formulas for calculating the shear stress τ and normal stress σ at the base of variable-thickness granular debris masses in states of static or dynamic equilibrium on slopes. The formulas include a lateral pressure coefficient κ, but use of a fixed value $\kappa = 0.7$ yields predictions of σ that on average err by less than 3% and of τ that on average err by less than 13% in matching basal stresses measured in six large-scale experiments involving wet debris masses with varying geometries and compositions. Much larger prediction errors result from use of infinite-slope or shallow-debris approximations. Specialized versions of the new formulas apply if basal topography is discretized and represented by a "staircase" function in a digital elevation model. Use of these formulas to assess static limiting equilibrium conditions shows that the apparent basal Coulomb friction angle ϕ_{tread} of debris that engages friction acting on the horizontal surfaces (or "treads") of a staircase sloping at an angle θ is generally described by $\tan\phi_{tread} = \tan(\phi - \theta) + \kappa \tan\theta$, where ϕ is the true basal friction angle of the same debris in contact with a uniformly sloping bed. Differences between the values of ϕ and ϕ_{tread} can greatly influence the results of numerical simulations that use unsmoothed digital elevation model topography to calculate the stability or dynamics of debris masses on slopes.

1. Introduction

Calculations of stresses that act on the base of sloping granular debris masses serve several important purposes. For example, calculations of basal shear stress are necessary for evaluating the balance of forces that controls downslope debris acceleration, irrespective of whether the debris mass is in motion or at rest. They are also required for assessing the potential for bed erosion and for evaluating the propensity of moving debris to radiate seismic energy into the bed. Calculations of basal normal stress are equally important—in part because normal stress limits shear stress when basal Coulomb friction is fully engaged (i.e., when $\tau = \sigma \tan\phi$ is satisfied, where τ is basal shear stress, σ is basal normal stress, and ϕ is a basal friction angle that implicitly accounts for pore pressure effects). However, except in one-dimensional problems, no method exists for calculating τ and σ exactly because the governing balance equations are insufficient for determining two- and three-dimensional stress states. Thus, for 2-D and 3-D geometries, constitutive assumptions or other analogous assumptions are required to obtain analytical formulas or numerical results that estimate values of τ and σ.

In this paper we describe the derivation, implementation, and experimental testing of new algebraic formulas for estimating shear and normal stresses at the base of 2-D debris masses in states of static or dynamic mechanical equilibrium on slopes. (In disequilibrium states these basal stresses can be modified by accelerations that change the apparent weight of the debris, but that is a distinct topic which we do not address in this paper.) Our new formulas include a single, depth-averaged tuning parameter, a lateral pressure coefficient denoted by κ. We show that for the debris geometries and compositions in our experiments, a fixed value $\kappa = 0.7$ yields estimates of τ, σ, and τ/σ that are more accurate than estimates obtained from widely used infinite-slope and shallow-debris equations.

Our new basal stress formulas can be implemented precisely in depth-averaged models that employ Earth-centered, rectangular Cartesian coordinates, irrespective of the steepness of local bed or surface slopes. However, specialized versions of the formulas apply if conventional, unsmoothed digital elevation models (DEMs) are used to depict topographic and basal slip surfaces as "staircase" functions that have constant elevation values in individual DEM cells. Such staircase surfaces represent mathematical abstractions rather than real physical surfaces, but they are nonetheless relevant because DEMs provide the

baseline topographic data for many numerical simulations of mass movements. Indeed, computations that use DEM data directly to compute τ, σ, and τ/σ can hold practical advantages over computations that require preliminary processing to smooth the DEM data. DEM staircase topography is especially well suited for use in numerical simulations that employ finite-volume solution methods and computational cells that coincide with DEM cells. Moreover, use of unsmoothed DEM topography may have its greatest advantages in finite-volume computations that employ adaptive mesh refinement to facilitate efficient numerical simulations in large domains, which may include billions of DEM cells (LeVeque et al., 2011). In such cases use of unsmoothed DEM data eliminates the need to recompute base topography as the computational grid evolves (e.g., George et al., 2017; Iverson & George, 2016).

Our specialized basal stress formulas for staircase topography lead to the inference that the apparent basal Coulomb friction angle of debris resting on flat-bottomed DEM cells differs from the Coulomb friction angle of the same debris in contact with a smoothly sloping bed. The difference arises from a purely geometric effect associated with use of a vertically depth-averaged stress state and staircase topography, and it does not imply that any revisions are warranted in physical theories of static or rate-dependent Coulomb friction. On the other hand, the distinction between true and apparent Coulomb friction is relevant regardless of the particular friction theory employed.

2. Context

To place our new basal stress equations in context, it is useful first to review some key features of some well-established basal stress equations. For example, the widely used infinite-slope equations apply to an infinitely extensive planar slab of material that has a uniform bed-normal thickness, h, uniform vertical thickness, H, and uniform angle of inclination, $\beta = \theta$, where β is the surface slope angle and θ is the basal slope angle. In this case the stress state is strictly one-dimensional, and the basal normal stress and shear stress obey the equations

$$\sigma = \rho g h \cos\theta = \rho g H \cos^2\theta \tag{1}$$

and

$$\tau = \rho g h \sin\theta = \rho g H \cos\theta \sin\theta, \tag{2}$$

in which ρ is the debris bulk density and g is the magnitude of gravitational acceleration. These infinite-slope basal stress equations are exact, but only if every geometrical assumption noted above is satisfied. However, they also provide zero-order approximations for cases in which the debris geometry is more complex.

For a layer of debris of smoothly varying thickness $h(x)$, a widely used first-order correction to the infinite-slope basal shear stress equation (2) is obtained by integrating a 2-D Cauchy stress field equation through the debris thickness and assuming that the longitudinal normal stress is proportional to the 1-D geostatic basal normal stress defined by (1) (e.g., Savage & Hutter, 1989). Appendix A explains the details of this procedure, which yields the result

$$\tau = \rho g h \sin\theta - \kappa\, \rho g h \cos\theta (\partial h/\partial x), \tag{3}$$

where x is a bed-parallel coordinate pointing in the direction of steepest descent and κ is a lateral pressure coefficient that satisfies $\kappa = 1$ if the stress state is hydrostatic but may differ significantly from 1 for either dry or wet granular debris (Iverson & Denlinger, 2001; Hungr, 2008; Savage & Hutter, 1989).

Precise definitions and values of κ can be specified if particular constitutive assumptions are used (such as Coulomb yield behavior or linearly elastic behavior), but here we avoid such assumptions and treat κ simply as a tuning parameter. This treatment makes our definition of κ similar to that of an "Earth pressure coefficient at rest," as is commonly employed in soil mechanics (e.g., Fang et al., 1997). However, our usage of κ departs somewhat from soil mechanics convention because in (3) κ implicitly includes the effects of intergranular fluid as well as solid grains.

Shallow-debris scaling shows that the correction term containing $\partial h/\partial x$ in (3) is of order $\widehat{h}/\widehat{l}$, where $\widehat{h}$ is the characteristic slope-normal thickness of a finite debris mass and $\widehat{l}$ is its characteristic slope-parallel length (Savage & Hutter, 1989). As $\widehat{h}/\widehat{l}$ approaches 0, the correction term containing $\partial h/\partial x$ generally has

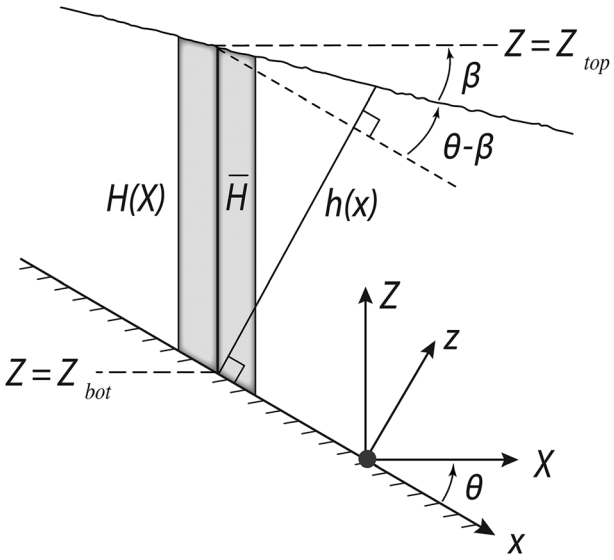

Figure 1. Schematic cross-sectional geometry of a vertical column of debris (shaded) contained within a larger prism of debris resting on a bed sloping at an angle θ with respect to the horizontal X axis. The column's local vertical thickness is $H(X)$, and its mean vertical thickness is $\overline{H} = Z_{\text{top}} - Z_{\text{bot}}$. Its local bed-normal thickness is $h(x)$, and its surface slope angle is β, which generally differs from θ. Both the x-z and X-Z coordinates systems are shown.

increasing accuracy but diminishing importance. On the other hand, if $\widehat{h}/\widehat{l} \to 1$ applies, then the accuracy of the correction term generally degrades. An additional correction term must be added to (3) in applications that use a curvilinear x coordinate that is fitted to a smoothly curving bed (e.g., Bouchut et al., 2003; Keller, 2003; Savage & Hutter, 1991), but subsequent sections of this paper focus on applications that use rectilinear coordinates that are not aligned with the bed.

Although (3) is defensible from a theoretical as well as practical perspective, it is by no means exact, and several important issues arise in its application to geophysical problems. The most basic of these issues stems from the fact that predictions of (3) have seldom, if ever, been subject to direct experimental tests that entail measurements of shear stresses beneath sloping masses of debris with spatially variable thicknesses. A second and equally fundamental issue is that models that employ the first-order correction term $-\kappa\rho g h \cos\theta(\partial h/\partial x)$ in calculations of τ commonly omit any analogous correction term in calculations of σ (e.g., Hungr, 2008; Iverson & Denlinger, 2001; Savage & Hutter, 1989). They instead employ the zero-order infinite-slope approximation expressed by (1). Consequently, values of τ/σ calculated to assess the potential engagement of basal Coulomb friction might err systematically due to an inconsistency in the methods used to estimate τ and σ. A third issue is that values of κ in (3) are generally poorly constrained—except by rather idealized theoretical considerations (e.g., Hungr, 2008; Iverson, 1997). Finally, an issue exists in geophysical applications that use topography discretized in DEMs of irregular terrain. In such applications the elevation of each DEM cell defines a horizontal surface (or "tread") in a staircase function, and on each tread surface $\theta = 0$ locally applies. However, setting $\theta = 0$ in (1) and (3) does not account for the overall slope of the staircase topography, implying that additional mechanical effects must be considered. Subsequent sections of this paper address each of these issues by deriving and testing more-general formulas that can be used in place of (1) and (3).

3. Mechanics

Our derivation employs a Cartesian coordinate system in which Z is vertical and X is horizontal, as is used in most DEMs. It considers basal stresses produced by balanced forces acting on a vertical column of debris of variable thickness, $H(X)$, where X lies within the same vertical plane as Z and the slope-parallel coordinate, x (Figure 1). Although the derivation considers a 3-D debris column, it assumes that forces acting normal to the vertical plane depicted in Figure 1 have no net effect on mechanical equilibrium of the column, and in this sense it assumes that a two-dimensional stress state applies. It also omits shear stresses on the vertical sides of the column that might act to distort it as well as rotational moments that might act to topple it. Our derivation consequently focuses on the potential for purely translational motion of the column parallel to a locally planar bed sloping at an angle θ (Figure 1). (In Appendix B we derive additional equations that describe moment equilibrium that governs the potential for rotational motion and consequent toppling of the column. For realistic values of physical variables, the equations imply that translational motion generally supersedes rotation.)

3.1. Basal Stress Equations

Our analysis focuses on basal stresses that develop in reaction to vertical forces caused by the weight of overlying material and horizontal forces exerted by adjacent debris upslope and downslope. It assumes that each of these forces is proportional to the depth-averaged debris bulk density defined by

$$\rho = \frac{1}{\overline{H}} \int_{Z_{\text{bot}}}^{Z_{\text{top}}} \left[\rho_s(1-n) + \rho_f n\right] \mathrm{d}Z, \tag{4}$$

where $\overline{H}$ is the mean vertical thickness of a debris column with a mean base elevation Z_{bot} and mean surface elevation Z_{top}, ρ_s is the mass density of solid grains, ρ_f is the mass density of pore fluid (including both water

and air), and n is the debris porosity (Figure 1). The weight W of the column is given by $W = \rho g \overline{H} A$, where g is the magnitude of gravitational acceleration and A is the horizontal cross-sectional area of the column. The contributions of W to the basal normal stress σ and basal shear stress τ are found by resolving W into bed-normal and bed-parallel components and dividing each of these components by the area of the planar bed surface contacted by the column, $A/\cos\theta$, where θ is the angle of bed inclination. Thus, the contributions of W to σ and τ are given by

$$\sigma_W = \rho g \overline{H} \cos^2\theta \tag{5}$$

and

$$\tau_W = \rho g \overline{H} \cos\theta \sin\theta. \tag{6}$$

If the debris thickness H is constant, such that $H = \overline{H}$ applies everywhere, then these basal stress state equations reduce to the infinite-slope equations, (1) and (2).

If the value of H differs on the upslope and downslope faces of the column, then σ and τ are influenced by a net horizontal force exerted by adjacent material upslope and downslope. The weight of this material produces a depth-averaged lateral pressure against vertical faces of the column that can be expressed as $(1/2)\kappa\rho g H$, where κ is a lateral pressure coefficient. This pressure exerts a local depth-averaged horizontal normal force $F = (1/2)\kappa\rho g H^2 B$, where B is the cross-slope breadth of the column and HB is the surface area of a vertical face of the column, which is normal to X. Thus, if $H(X)$ is continuously differentiable, then the net horizontal force acting on the column is expressed by $F_{\text{net}} = -\partial[(1/2)\kappa\rho g H^2 BL]/\partial X$, where L is the horizontal length of the column in the X direction, such that $BL = A$ applies. If the values of κ, ρ, g, B, L, and θ are not functions of X, then the expression for F_{net} reduces to $F_{\text{net}} = -\kappa\,\rho g A \overline{H}(\partial H/\partial X)$, which can also be written as $F_{\text{net}} = -\kappa\,\rho g A \overline{H}(\tan\theta - \tan\beta)$, where β is the local angle of inclination of the surface slope (Figure 1). The contributions of F_{net} to σ and τ are found by resolving F_{net} into bed-normal and bed-parallel components and dividing these components by the area of the sloping basal surface contacted by the column, $A/\cos\theta$. The contributions of F_{net} to σ and τ are thus found to be

$$\sigma_F = \kappa\rho g \overline{H} \cos\theta \sin\theta(\tan\theta - \tan\beta) \tag{7}$$

and

$$\tau_F = -\kappa\rho g \overline{H} \cos^2\theta(\tan\theta - \tan\beta). \tag{8}$$

The total normal stress σ and total shear stress τ acting on the sloping base of the column are given by the sums $\sigma = \sigma_W + \sigma_F$ and $\tau = \tau_W + \tau_F$. Use of (5)–(8) to evaluate these sums yields

$$\sigma = \rho g \overline{H} \cos\theta[\cos\theta + \kappa \sin\theta(\tan\theta - \tan\beta)] \tag{9}$$

and

$$\tau = \rho g \overline{H} \cos\theta[\sin\theta - \kappa \cos\theta(\tan\theta - \tan\beta)]. \tag{10}$$

These are our new basal stress equations, which we have also derived by using a more rigorous—but lengthier—method that involves integrating the boundary stresses around the perimeter of the shaded domain shown in Figure 1. The equations indicate that positive longitudinal thickness gradients, which are expressed by $\tan\theta - \tan\beta > 0$ (or, equivalently, by $\partial H/\partial X > 0$), act simultaneously to increase basal normal stress and reduce basal shear stress.

For a special case in which the upper surface of the debris is horizontal (i.e., $\beta = 0$), (9) and (10) reduce to

$$\sigma = \rho g \overline{H}\left(\cos^2\theta + \kappa \sin^2\theta\right) \tag{11}$$

and

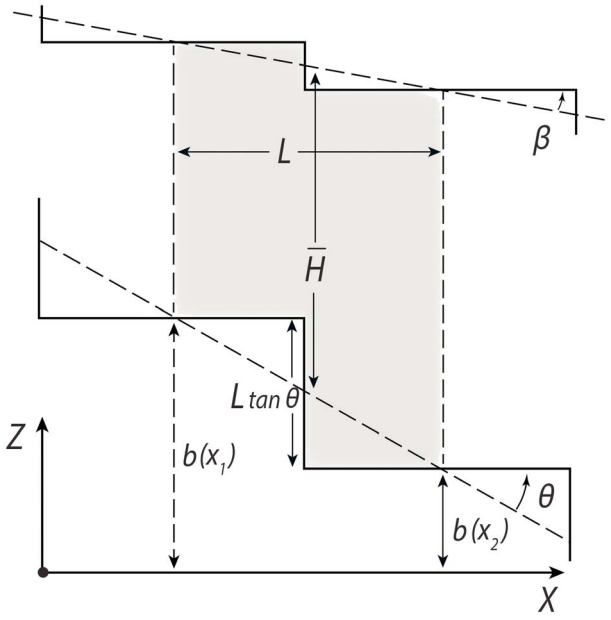

Figure 2. Schematic cross-sectional geometry of a vertical column of debris (shaded) that is bounded at its base and surface by digital elevation model staircase topography. The column rests on half of each of two adjacent staircase treads. The horizontal treads and the column each have length L in the X direction. The vertical height of the staircase riser separating two adjacent treads is given by $b(X_1) - b(X_2) = L \tan\theta$, where $b(X)$ is the local tread elevation and θ is the angle of the basal staircase slope. The mean ground surface slope angle is β, which generally differs from θ.

$$\tau = (1-\kappa)\rho g\overline{H}\cos\theta\sin\theta. \quad (12)$$

These equations predict that $\sigma = \rho g\overline{H}$ and $\tau = 0$ apply for a hydrostatically stressed mass (i.e., with $\kappa = 1$), regardless of the bed slope angle. However, they predict that a more complex basal stress state exists if $\kappa \neq 1$ as well as $\beta = 0$ applies.

Another consideration in use of (9) and (10) arises from the fact that predicted values of σ become negative if the condition $\tan\beta > \tan\theta + 1/(\kappa\tan\theta)$ applies and predicted values of τ become negative if the condition $\tan\beta < \tan\theta - (1/\kappa)\tan\theta$ applies. Negative τ values merely indicate that the basal shear stress imposed by debris with a sufficiently steep adverse surface slope acts in the negative x direction of Figure 1. On the other hand, negative σ values are physically implausible unless the debris is bonded to its bed by cohesion. Debris geometries that lead to conditions with $\sigma < 0$ are quite atypical, however. Graphs of the equation $\tan\beta = \tan\theta + 1/(\kappa\tan\theta)$ show that for $\kappa = 1$ (which is the maximum plausible value of κ in many circumstances, as discussed in section 3.4), a condition with $\sigma < 0$ can exist only if $\beta > 63^\circ$ applies, which describes a debris surface slope that is steeper than the maximum slope generally attainable by granular debris. Failure by toppling (due to violation of moment equilibrium) can also preclude the development of such steep surface slopes (Appendix B).

3.2. Relationship of (9) and (10) to (1) and (3)

The physical implications of (9) and (10) are distinct from those of (1) and (3). Unlike derivations of (1) and (3), our derivation of (9) and (10) involves no assumptions that restrict the magnitudes of the slope angles θ and β, or of their difference, $\theta - \beta$. Consequently, (9) and (10) cannot be obtained from (1) and (3) through use of a coordinate transformation. Instead, the derivation of (9) and (10) involves the specific set of assumptions described in the preceding paragraphs.

The shallow-debris basal stress equations, (1) and (3), provide approximations of (9) and (10) that become better as longitudinal gradients in debris thicknesses become smaller. The geometric relationships illustrated in Figure 1 indicate that the exact expressions $h = H[\cos\theta + \sin\theta\tan(\theta - \beta)]$ and $\partial h/\partial x = \tan(\theta - \beta)$ can be used to rewrite (1) and (3) with H rather than h as the dependent variable. However, the resulting forms of (1) and (3) match (9) and (10) only in the limit $\theta - \beta \to 0$. Use of the first-order correction term in (3), $-\kappa\rho gh\cos\theta(\partial h/\partial x)$, nevertheless bolsters that equation's accuracy in approximating (9), particularly if the value of $\theta - \beta$ is small enough that $\partial h/\partial x = \tan(\theta - \beta) \approx \tan\theta - \tan\beta$ applies.

3.3. Implementation of (9) and (10) With DEM Topography

Equations (9) and (10) provide estimates of stresses acting on a basal boundary surface sloping at any angle, but use of the equations in numerical simulations involves an additional consideration if sloping basal topography with diverse elevations $b(X)$ is represented by a series of discrete steps, as it is in a DEM (Figure 2). Collectively the discrete steps form a sloping staircase function, but each individual step has a horizontal surface (i.e., a staircase tread) on which $b(X)$ is constant and $\theta = 0$ locally applies. Thus, on individual horizontal treads, (9) and (10) reduce to $\sigma_{ZZ} = \rho g H_m$ and $\tau_{ZX} = \kappa\rho g H_m \tan\beta$, where the subscripts ZZ and ZX indicate that σ_{ZZ} and τ_{ZX} act on horizontal tread surfaces that are normal to Z, and H_m denotes the mean vertical thickness of debris overlying an individual tread. (Note that for consistency the ground surface topography illustrated in Figure 2 is also depicted as a staircase function, but the form of this function has no effect on our basal stress calculations because the ground surface is treated as a stress-free boundary, irrespective of its shape.)

If a prism of debris rests on half of each of two adjacent treads and thereby spans a representative section of the staircase slope (i.e., the shaded region in Figure 2), then integrating the equations $\sigma_{ZZ} = \rho g H_m$ and

$\tau_{ZX} = \kappa\rho g H_m \tan\beta$ in the X direction across this span shows that the total boundary normal force F_{ZZ} and boundary shear force F_{ZX} exerted *on* the debris prism *by* the treads are given by

$$F_{ZZ} = \rho g \overline{H} L B \tag{13}$$

and

$$F_{ZX} = -\kappa\rho g \overline{H} L B \tan\beta, \tag{14}$$

where $\overline{H}$ is the mean thickness of the debris prism overlying the two treads, L is the prism length, and B is its cross-slope breadth—geometric definitions that are the same as those used in the derivation of (9) and (10).

Two additional forces influence the mechanical equilibrium of a prism of debris resting on half of each of two adjacent treads of a sloping staircase (Figure 2). One is the net horizontal driving force due to the difference in pressures acting on the upslope and downslope faces of the prism, F_{net}. The analysis in section 3.1 showed that this force is described by

$$F_{\text{net}} = -\kappa\rho g \overline{H} L B(\tan\theta - \tan\beta). \tag{15}$$

The other force is a horizontally acting normal force exerted by the vertical staircase surface that joins the two adjacent treads, known as a staircase "riser" (Figure 2). This force is described by

$$F_{XX} = \kappa\rho g \overline{H} L B \tan\theta, \tag{16}$$

where $\kappa\rho g\overline{H}$ is the mean value of the horizontal normal stress exerted by the riser, $LB\tan\theta$ is the surface area of the riser, and $\tan\theta$ is the mean staircase slope averaged over the horizontal distance L (Figure 2). Equation (16) shows that the force F_{XX} partially counteracts F_{net}. As a consequence, the total horizontal driving force acting on the vertical surfaces of the prism of debris shown in Figure (2) is found by adding (15) and (16) to obtain

$$F_{\text{tot}} = \kappa\rho g \overline{H} L B \tan\beta. \tag{17}$$

Thus, at mechanical equilibrium, the horizontal driving force given by (17) precisely counteracts the horizontal basal shear force given by (14).

The system of basal boundary forces described by (13), (14), and (16) is consistent with the basal stresses described by (9) and (10). This consistency can be demonstrated by considering a system of boundary forces that are equivalent to (13), (14), and (16) but which act on a basal boundary sloping uniformly at the angle θ. These forces are found by resolving the force vectors F_{ZZ}, F_{ZX}, and F_{XX} into components acting normal and parallel to the sloping boundary and summing their contributions to obtain the total boundary normal force

$$F_{\text{normal}} = F_{ZZ}\cos\theta - F_{ZX}\sin\theta + F_{XX}\sin\theta \tag{18}$$

and shear force

$$F_{\text{shear}} = F_{ZZ}\sin\theta + F_{ZX}\cos\theta - F_{XX}\cos\theta. \tag{19}$$

Substituting (13), (14), and (16) into (18) and (19) then yields

$$F_{\text{normal}} = \rho g \overline{H} L B[\cos\theta + \kappa\sin\theta(\tan\theta - \tan\beta)] \tag{20}$$

and

$$F_{\text{shear}} = \rho g \overline{H} L B[\sin\theta - \kappa\cos\theta(\tan\theta - \tan\beta)]. \tag{21}$$

Finally, if F_{normal} and F_{shear} are converted to stresses by dividing (20) and (21) by the surface area of the sloping surface on which the forces act, $LB/\cos\theta$, then the resulting equations match (9) and (10) exactly.

The foregoing analysis demonstrates two important points. First, (13) and (14) provide suitable descriptions of the basal normal and shear forces that act on the horizontal treads of sloping staircase topography as portrayed in DEMs. The equations apply at any scale—regardless of how finely staircase topography is discretized. Equally important, (9) and (10) provide compatible descriptions of the stresses that act on a smoothly sloping bed that is not discretized as a staircase.

3.4. Constraints on κ Values

The lateral pressure coefficient κ appears in many of the preceding equations and characterizes the combined effects of the debris' solid and fluid constituents on horizontal normal stresses. The solid and fluid constituents generally have distinct influences on κ, and these influences can differ for static and deforming states. Here we define κ as the ratio of the depth-averaged steady state horizontal total normal stress, $(1/2)\kappa\rho gH$, to the depth-averaged steady state vertical total normal stress, $(1/2)\rho gH$.

To estimate values of κ for static or quasi-static solid-fluid debris mixtures, we first relate κ to the lateral stress coefficient for a single-phase granular solid, κ_s. Following the rationale of Iverson and Denlinger (2001), which employs Terzaghi's effective-stress principle for water-saturated granular debris (Lade & De Boer, 1997), we use the relationship

$$\kappa = \kappa_s\left(1-\frac{p}{\rho gH}\right)+\frac{p}{\rho gH}, \tag{22}$$

where p denotes the basal pore-fluid pressure. This equation implies that the granular solid phase produces a depth-averaged lateral effective stress equal to $(1/2)\kappa_s(1-p)\rho gH$, while the fluid phase produces a depth-averaged lateral stress equal to $(1/2)p$. For fully liquefied states with $p=\rho gH$, (22) reduces to $\kappa=1$, and for fully dewatered states with $p=0$, it reduces to $\kappa=\kappa_s$.

The implications of (22) can be clarified further by considering a case in which the basal pore pressure is hydrostatic (i.e., $p=\rho_f gH$) and (22) reduces to $\kappa=\kappa_s+(1-\kappa_s)(\rho_f/\rho)$. Combining this equation with the definition of ρ given in (4) leads to the result

$$\kappa=\frac{\kappa_s\left[(1-n)\left(\rho_s-\rho_f\right)/\rho_f\right]+1}{\left[(1-n)\left(\rho_s-\rho_f\right)/\rho_f\right]+1}. \tag{23}$$

The plausible range of κ values described by (23) is quite well constrained. Extensive experimentation by Fang et al. (1997) has shown that the full-scale range of κ_s values for sloping prisms of loose granular materials at rest—without fully engaged frictional resistance—is approximately 0.2 to 1. The range of plausible values of $(1-n)(\rho_s-\rho_f)/\rho_f$ for typical grain-water mixtures mantling slopes on Earth's surface is roughly 0.4 to 1.2. Use of these ranges of parameter values in (23) shows that the most plausible values of κ for the sediment-water debris mixtures used in our experiments range from roughly 0.5 to 1.

4. Experimental Methods and Materials

Six large-scale experiments conducted at the USGS debris-flow flume in 2016 afforded an opportunity to test the predictions of (9) and (10). In three pairs of replicate experiments, we used a diesel-powered front-end loader and manual shoveling to place prisms consisting of either 10 or 8 m^3 of static, loose, moist debris behind a vertical steel headgate near the top of the flume, which slopes at an angle $\theta=31^\circ$ (Figure 3). The 10-m^3 debris prisms were distinguished from the 8-m^3 debris prisms mostly by their steeper surface slopes ($\beta=17^\circ$ for the 10-m^3 prisms versus $\beta=9^\circ$ for the 8-m^3 prisms). Each debris prism was 1.9 m high where it rested against the upslope face of the closed headgate, and each was approximately 4.7 m long where it contacted the flume bed, which consisted of broom-finished concrete with a surface texture similar to that of standard sidewalks (Figure 3). The prisms were uniformly 2 m wide and were bounded laterally by the vertical flume sidewalls, which consisted of smooth-finished concrete.

4.1. Debris Composition, Initial Bulk Density, and Initial Water Content

Each experiment used a sand-gravel (SG) debris mixture composed of 66% well-rounded gravel, 33% river sand, and 1% finer grains by dry weight. Iverson et al. (2010) provided a detailed characterization of the

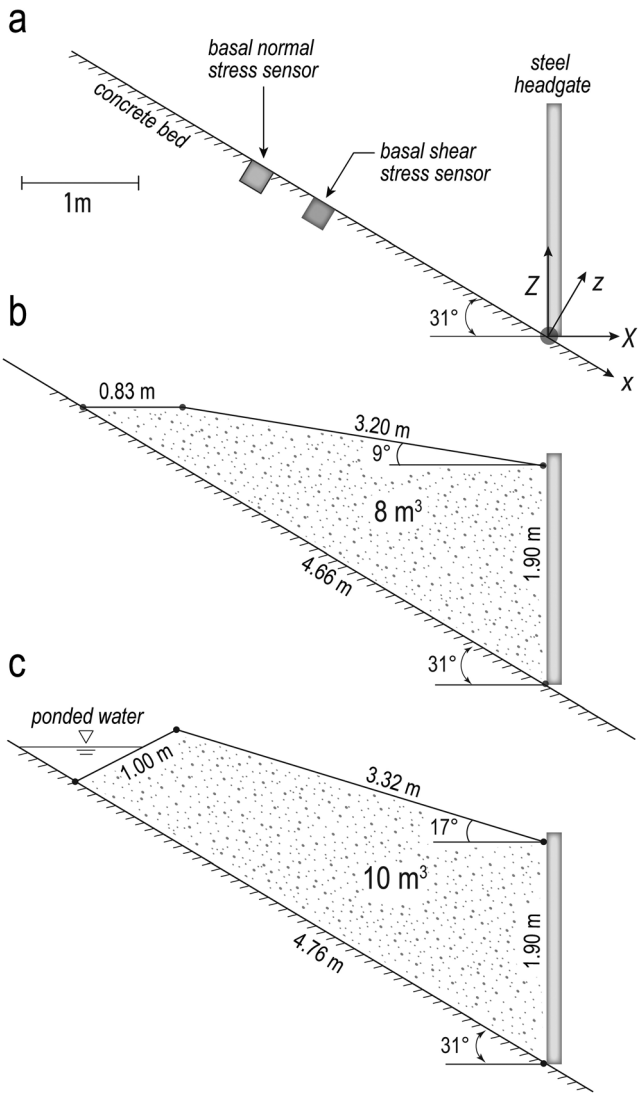

Figure 3. Schematic vertical cross-sectional geometries of (a) the flume headgate area, (b) the 8-m^3 debris prisms, and (c) the 10-m^3 debris prisms used in the experiments. The centroids of the flush-mounted sensor plates used to measure basal shear stress and basal normal stress were located at $x = -2.23$ m and $x = -2.85$ m, respectively, where x is aligned parallel to the flume bed.

grain-size distribution and geotechnical properties of this SG mixture, which had a static internal friction angle $\phi_{int} = 39.3 \pm 3°$ and a static basal friction angle $\phi_{bed} = 28 \pm 0.8°$ on the broom-finished concrete bed. The sand-sized grains in the debris consisted of rock fragments with diverse mineralogical compositions representative of their provenance in the varied geologic terranes of the Willamette River watershed upstream from Eugene, Oregon. We assumed that $\rho_{sand} = 2{,}650$ kg/m^3 was a suitable value for the mean density of these and finer grains. The gravel clasts consisted of 85% basalt and 15% pyroclastic and metasedimentary rocks by mass. We made measurements on 109 compositionally representative gravel clasts using a Mettler Toledo Excellence XP/XS density kit, which yielded a mean and standard deviation density $\rho_{grav} = 2{,}503 \pm 196$ kg/m^3 for these grains.

The debris mixture used in two of the experiments also included approximately 560 randomly positioned angular cobbles, which we added during placement of the debris behind the flume headgate (Table 1). The individual cobbles had mean volumes of 0.00024 m^3 and mean masses of 0.56 kg, based on measurements of 93 individual clasts. In our calculations of debris bulk density and porosity, we disregarded the presence of these cobbles, because they were not included in our bulk density samples and they collectively represented a total volume of only ~0.13 m^3 in each experiment. Nevertheless, the presence of the cobbles was noteworthy from a mechanical standpoint.

We determined the bulk densities and water contents of the initially moist SG debris mixtures positioned behind the headgate by using the excavation, drying, and weighing technique detailed by Iverson et al. (2010). A total of 24 samples (four per experiment) were analyzed to obtain a mean and standard deviation dry bulk density $\rho_{dry} = 1{,}583 \pm 157$ kg/m^3 and a mean and standard deviation gravimetric water content $w_g = 0.061 \pm 0.011$ (Table 1). These quantities are used to calculate the mean debris porosity n and mean volumetric water content w_v from the easily derived formulas

$$n = 1 - \left(\frac{\rho_{dry}}{\rho_{sand}} \frac{M_{sand}}{M_{dry}} + \frac{\rho_{dry}}{\rho_{grav}} \frac{M_{grav}}{M_{dry}} \right) \tag{24}$$

and

$$w_v = \frac{\rho_{dry}}{\rho_f} w_g, \tag{25}$$

where M_{dry} is the dried sample mass, $M_{sand}/M_{dry} = 0.34$ is the mass fraction of sand and finer sediment in the dried SG mixture, $M_{grav}/M_{dry} = 0.66$ is the mass fraction of gravel clasts in the dried mixture, $\rho_f = 1{,}000$ kg/m^3 is the mass density of water, $\rho_{sand} = 2{,}650$ kg/m^3 is the sand gain density, and $\rho_{grav} = 2{,}503$ kg/m^3 is the gravel grain density. Use of these values in (24) and (25) along with the data summarized in Table 1 yields a mean debris porosity $n \approx 0.38$ and mean volumetric water content $w_v \approx 0.096$. Thus, roughly 25% of the pore space in the initially moist SG samples was filled with water.

4.2. Debris Wetting, Final Bulk Density, and Final Water Content

After placement and sampling of the debris prisms, we wetted them by applying water via metered subsurface conduits and surface sprinklers. Our goal was to establish completely saturated debris prisms with sloping water tables coincident with the prisms' upper surfaces. This goal was realized in the experiments with 8-m^3 debris prisms, but it was more difficult to attain in the experiments with 10-m^3 debris

Table 1
Bulk Densities, Porosities, and Water Contents of Debris Samples (Four per Experiment) Collected After Placing Debris Behind Flume Headgate but Prior to Adding Water

Experiment date, initial debris volume, and debris composition[a]	Moist bulk density, mean and standard deviation (kg/m^3)	Dry bulk density ρ_{dry}, mean and standard deviation (kg/m^3)	Gravimetric water content[b] w_g, mean and standard deviation	Mean porosity n	Mean volumetric water content w_v	Mean percent saturation of porosity
14 June 2016, 8 m^3, SG	1,842 ± 111	1,740 ± 99	0.059 ± 0.0038	0.32	0.10	31
15 June 2016, 8 m^3, SG	1,516 ± 108	1,408 ± 90	0.076 ± 0.0087	0.45	0.11	24
16 June 2016, 8 m^3, SG + cobbles	1,588 ± 115	1,498 ± 108	0.060 ± 0.0085	0.41	0.090	22
21 June 2016, 8 m^3, SG + cobbles	1,626 ± 98	1,525 ± 92	0.065 ± 0.0018	0.40	0.099	25
22 June 2016, 10 m^3, SG	1,837 ± 29	1,760 ± 27	0.042 ± 0.0026	0.31	0.074	24
23 June 2016, 10 m^3, SG	1,665 ± 114	1,568 ± 110	0.061 ± 0.0040	0.39	0.096	25
Mean values for 24 samples	1,679 ± 158	1,583 ± 157	0.061 ± 0.011	0.38	0.095	25

[a]"SG" denotes a sand-gravel sediment mixture that was characterized in detail by Iverson et al. (2010); "cobbles" are characterized in detail in this paper.
[b]Gravimetric water content is defined as mass of water divided by mass of dry solid grains.

prisms owing to their steeper surface slopes. Thus, surficial layers of partially saturated debris that averaged several centimeters in thickness persisted in the 10-m^3 debris prisms. On the other hand, the 10-m^3 debris prisms also developed ponds at their upper ends, which each contained about ~0.3 m^3 of standing water (Figure 3c).

As a sloping water table developed in each debris prism, effluent groundwater began to pool against the upper face of the headgate. Metered drainage of this pooled water occurred through ports installed near the top of the headgate, but no other significant drainage occurred as water was applied. Data and simple calculations therefore yielded complete volumetric water budgets for the debris prisms (Table 2). In constructing these water budgets, it was necessary to account for the initial ambient water content of the loosely packed debris as well as its subsequent settlement during water application.

Spot measurements along the flume sidewalls indicated that settlement caused a ~6% reduction in the total volume of each debris prism during watering. This 6% reduction in total volume implies that a 6% increase occurred in the mean dry bulk density ρ_{dry} and that a 10% reduction occurred in the mean total porosity n. From these modifications we infer that the mean values $\rho_{dry} \approx 1{,}678$ kg/m^3 and $n \approx 0.34$ applied after watering of the debris was completed. Taken in conjunction with the volumetric water contents listed in the last column of Table 2, the value $n \approx 0.34$ also implies that the settled debris prisms were almost entirely saturated with water. The settled debris with $\rho_{dry} \approx 1{,}678$ kg/m^3 and $n \approx 0.34$ would have had a total bulk density $\rho = \rho_{dry} + n\rho_f \approx 2{,}018$ kg/m^3 if it had been 100% saturated with water having a density $\rho_f = 1{,}000$ kg/m^3. We consequently adopt the rounded and slightly smaller value $\rho = 2{,}000$ kg/m^3 as suitable for purposes of calculating theoretical values of basal stresses.

4.3. Basal Stress Measurements

We made measurements of basal stresses using Omega Model LC S-beam load cells that were rigidly coupled to 500-cm^2 circular steel plates that served as the sensing elements in contact with basal debris. The normal stress sensors had a relatively simple configuration like that illustrated by Major and Iverson (1999), but the shear stress sensors had a more complex configuration that used roller bearings to mechanically decouple shear loads from normal loads (Figure 4). Each sensor plate was mounted flush with the flume bed and was roughened with a sand-textured finish to match the roughness of the adjacent concrete bed. The plates were also fitted with soft rubber gaskets along their perimeters to inhibit jamming with sediment.

The shear- and normal-stress sensors were each installed along the flume centerline, but they were positioned at slightly different distances upslope from the flume headgate. Measured parallel to the flume bed, the shear-stress sensor was centered at $x = -2.23$ m while the normal-stress sensor was centered at $x = -2.85$ m, where negative values of x indicate distances upslope from the foot of the headgate (Figure 3). As a result of these differing sensor positions, the shear- and normal-stress sensors had different burial depths. Measured vertically, these depths initially were 0.82 m for the normal-stress sensor and 1.06 m for the shear-stress sensor beneath the 8-m^3 sediment prisms, and they were 1.18 m for the normal-stress sensor and 1.34 m for the shear-stress sensor beneath the 10-m^3 debris prisms. However, after settlement

Table 2
Volumetric Data Summarizing Prewatering and Postwatering States of Debris Prisms

Experiment date	Debris composition[a]	Initial volume of loaded debris (m^3)	Initial water volume in debris[b] (m^3)	Net volume of water added to debris[c] (m^3)	Settled debris volume after addition of water (m^3)	Debris volumetric water content (total water volume ÷ settled debris volume) after water application
14 June 2016	SG	8.0	0.80	1.38	7.5	0.29
15 June 2016	SG	8.0	0.88	1.57	7.5	0.33
16 June 2016	SG + cobbles	8.0	0.72	1.70	7.5	0.32
21 June 2016	SG + cobbles	8.0	0.79	1.70	7.5	0.33
22 June 2016	SG	10.0	0.74	2.56	9.4	0.35
23 June 2016	SG	10.0	0.96	2.46	9.4	0.36

[a]"SG" denotes a sand-gravel sediment mixture that was characterized in detail by Iverson et al. (2010); "cobbles" are characterized in detail in this paper. [b]For each experiment initial water volumes were calculated from the mean water contents measured in four sediment samples, as summarized in Table 1. [c]Includes ~0.3 m^3 of ponded surface water in experiments of 22 June 2016 and 23 June 2016.

of the debris occurred in response to watering, these burial depths decreased by approximately 6 to 7 cm. The resulting final burial depths are listed in Table 3. Owing to irregularities in the settled sediment surface, the listed values might err by as much as ± 2 cm.

We calibrated the stress sensors in situ by placing a series of static weights directly on the sensor plates and accounting for the effect of the 31° bed slope and 500 cm^2 plate area when converting weights to stresses. During calibrations, the sensors were connected electronically to the same digital data acquisition system that was used to collect experimental data. We repeated the calibrations several times over the course of our experiments and found negligible drift of sensor output.

During both calibrations and experiments, we digitally logged the sensor output voltages at a sampling rate of 1,000 Hz. Then, following conversion of the logged voltages to physical units, we low-pass filtered the data using a time-domain digital RC filter with a cutoff frequency of 30 Hz. We subsequently decimated the filtered data to 100 Hz before we used a series of 500 data points to compute the mean values and standard deviations of the stress measurements we present here. The original, unfiltered 1,000-Hz data were archived by Iverson and Logan (2017) as part of a larger data set. The data we utilize here were collected during the time interval from $t = -5$ s to $t = 0$ s identified in that larger data set.

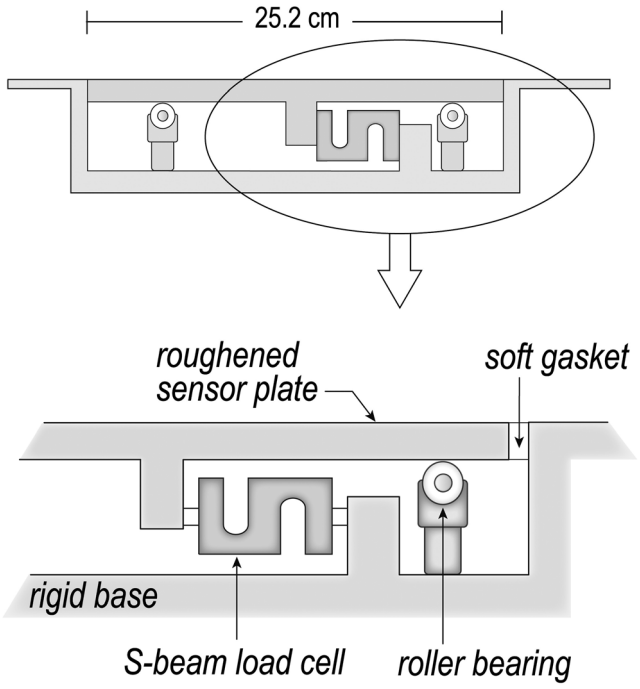

Figure 4. Schematic vertical cross sections illustrating the configuration of basal shear stress sensors viewed in a sloping reference frame aligned with the *x* coordinate of Figure 3.

5. Results

Our basal stress measurements, which are summarized in Table 3, generally exhibited a high degree of reproducibility between replicate pairs of experiments. The reproducibility was particularly good in view of the fact that the debris itself probably had variable packing configurations as a result of some randomness in the distributions of voids and force chains. As expected, the normal and shear stresses measured beneath the 10-m^3 debris prisms were significantly larger than those measured beneath the 8-m^3 debris prisms. In the experiments with 8-m^3 prisms, the debris containing large cobbles exerted stresses that were typically—but not universally—slightly larger than those exerted by the debris that lacked cobbles. These qualitative findings are consistent with expectations based on the thicknesses and compositions of the debris used in the various experiments.

5.1. Tests of Basal Stresses Predicted by (9) and (10)

Our most fundamental results compare the measured basal stress values listed in Table 3 with theoretical values of σ and τ predicted using equations (9) and (10). The predictions use the value $\rho = 2{,}000$ inferred from the measurements described in section 4.2, and they use the measured values of the geometric quantities listed in Table 3 for each experiment

Table 3
Measured Values of Basal Normal Stress, σ, Basal Shear Stress, τ, and Ancillary Geometric Quantities

Experiment date, initial debris volume, and debris composition	θ (deg)	β (deg)	Normal stress sensor depth, H_σ (m)	Measured value of $\sigma \pm 1$ standard deviation (Pa)	Shear stress sensor depth, H_τ (m)	Measured value of $\tau \pm 1$ standard deviation (Pa)
14 June 2016, 8 m^3, SG	31	9	0.76	12,949 ± 20	1.00	3,848 ± 20
15 June 2016, 8 m^3, SG	31	9	0.76	12,910 ± 20	1.00	4,664 ± 17
16 June 2016, 8 m^3, SG + cobbles	31	9	0.76	13,296 ± 19	1.00	4,849 ± 14
21 June 2016, 8 m^3, SG + cobbles	31	9	0.76	14,546 ± 18	1.00	4,651 ± 10
22 June 2016, 10 m^3, SG	31	17	1.11	18,078 ± 23	1.27	6,272 ± 28
23 June 2016, 10 m^3, SG	31	17	1.11	18,445 ± 29	1.27	6,237 ± 44

Note. H_σ and H_τ denote the postwatering vertical burial depths of the normal-stress sensor and shear-stress sensor, respectively.

and stress sensor. The suite of predictions uses lateral pressure coefficients ranging from $\kappa = 0$ (which reduces (9) and (10) to the infinite-slope equations (1) and (2)) to $\kappa = 1$ (which applies to a hydrostatically stressed debris mass). The range $0 \le \kappa \le 1$ also encompasses the range identified in section 3.4 as most physically plausible ($0.5 \le \kappa \le 1$). For this range of κ values, Figure 5a compares predicted and measured values of σ by plotting the prediction errors calculated using the formula

$$\text{percent error} = \frac{\sigma_{\text{pred}} - \sigma_{\text{meas}}}{\sigma_{\text{meas}}} \times 100, \tag{26}$$

where σ_{pred} and σ_{meas} denote the predicted and measured values of σ, respectively. An analogous formula is used to calculate the prediction errors for τ, which are plotted in Figure 5b.

The central finding illustrated in Figures 5a and 5b is that the value $\kappa = 0.7$ provides the best overall predictions of the measured values of σ and τ. This value of κ does not necessarily provide the best prediction of each individual measurement, but a mean error of only 2.8% results from using (9) with $\kappa = 0.7$ to predict measured values of σ, and a mean error of only 12.2% results from using (10) with $\kappa = 0.7$ to predict measured values of τ. No alternative value of κ yields such consistently accurate predictions. (We specify κ values with only single-digit precision because, in our view, the scatter of the data makes further refinement of κ values unwarranted.)

By contrast, very inaccurate predictions are obtained by disregarding the effect of the difference between the surface slope angle β and bed slope angle θ and instead using the infinite-slope approximation, which yields the results shown for $\kappa = 0$ in Figure 5. On average, the infinite-slope equations (1) and (2) yield predictions of σ that are too small by 16.3% and predictions of τ that are too large by 87.7%.

Finally, among the results illustrated in Figure 5a, one case constitutes a clear outlier that increases the mean prediction error: Predictions of the value of σ measured on 21 June 2016 are universally too small, regardless of the value of κ used in (9). For this case the prediction errors are so skewed and are also so inconsistent with other prediction errors summarized in Figure 5a that we believe the value of σ measured on 21 June 2016 was aberrant. A wide variety of possible explanations for this aberration exist, but a likely explanation is that one or more of the large cobbles present in the debris in this experiment lodged directly against the normal-stress sensor plate. Such lodgment could have resulted in a major force chain impinging on the plate and locally amplifying the basal normal stress. Such a possibility warrants caution when interpreting or calculating values of stresses at the base of heterogeneous debris masses.

5.2. Tests of Basal Stress Ratios Predicted by Alternative Models

Our experimental measurements of τ and σ provide data that enable tests of three sets of predictions of the basal stress ratio τ/σ, which holds particular significance owing to its role in evaluating basal Coulomb friction in granular masses. Each of the predictions takes into account that fact that the thickness of the debris where we measured τ, denoted by H_τ, differed from the thickness of the debris where we measured σ, denoted by H_σ. For these circumstances the infinite-slope equations (1) and (2) predict that

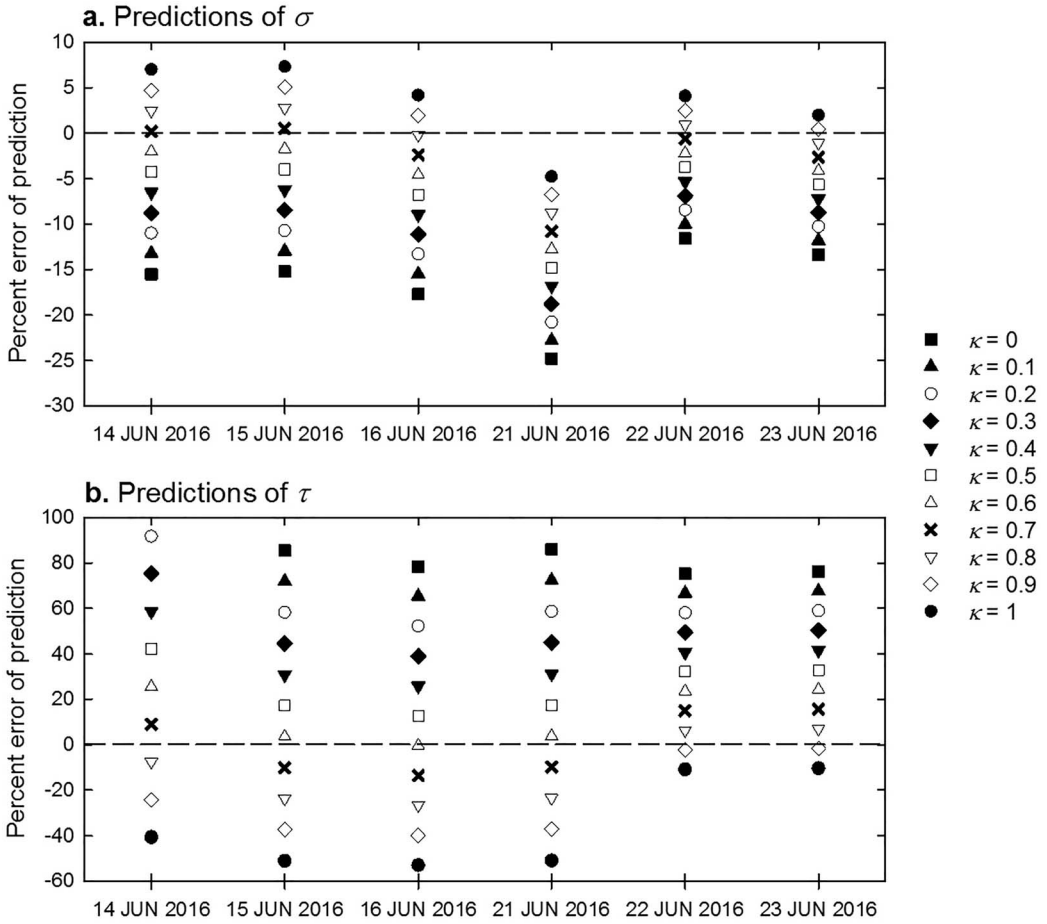

Figure 5. Percent error of basal stress predictions obtained by using equations (9) and (10) with values of κ ranging from 0 to 1. (a) Predictions of basal normal stress. (b) Predictions of basal shear stress. Predictions are shown for each of six experiments identified by date on the horizontal axes. However, for the experiment of 14 June 2016, prediction errors for τ calculated using $\kappa = 0$ and $\kappa = 0.1$ are not shown because they are off scale. In this case the errors are 125% and 108%, respectively.

$$\frac{\tau}{\sigma} = \frac{H_\tau}{H_\sigma} \tan\theta. \tag{27}$$

By contrast, equations (1) and (3), which include a first-order correction for the effect of small variations in debris thicknesses on τ but not on σ, predict that

$$\frac{\tau}{\sigma} = \frac{H_\tau}{H_\sigma} [\tan\theta - \kappa \tan(\theta - \beta)]. \tag{28}$$

Finally, equations (9) and (10), which include corrections for the effects of arbitrary variations in debris thicknesses on both τ and σ, predict that

$$\frac{\tau}{\sigma} = \frac{H_\tau}{H_\sigma} \left[\frac{\tan\theta - \kappa(\tan\theta - \tan\beta)}{1 + \kappa \tan\theta(\tan\theta - \tan\beta)} \right]. \tag{29}$$

We note that (29) reduces to (28) if σ is approximated by (1) and $\tan\theta - \tan\beta$ is approximated by $\tan(\theta - \beta)$. Furthermore, both (29) and (28) reduce to (27) if either $\kappa = 0$ or $\theta = \beta$ apply.

Comparisons of the values of τ/σ obtained from the data of Table 3 with values predicted by (27)–(29) demonstrate that (29) with $\kappa = 0.7$ yields the best overall match to the data (Figure 6). Moreover, use of

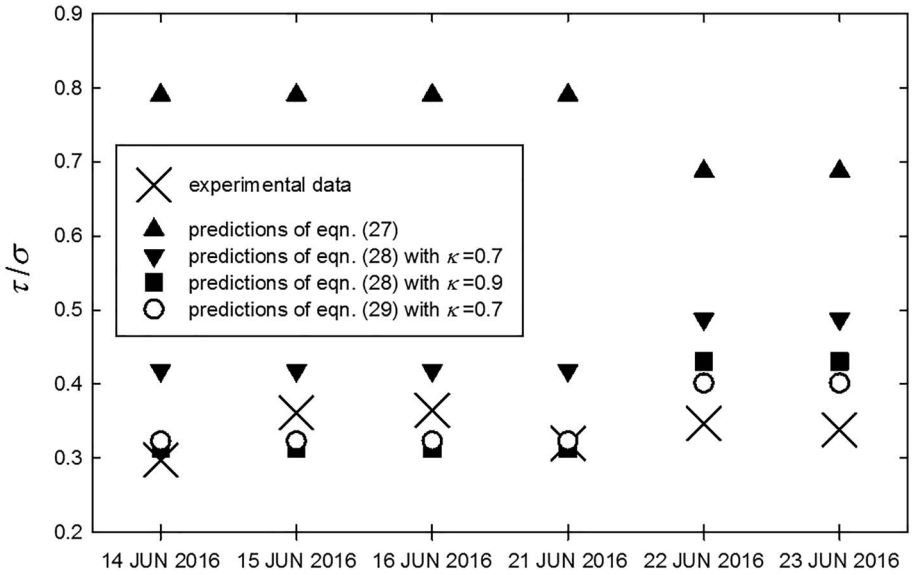

Figure 6. Comparisons of measured values of the basal stress ratio τ/σ with alternative predictions of τ/σ obtained using equations (27)–(29) and the values of geometric parameters listed in Table 3.

(29) with $\kappa = 0.7$ provides the most accurate prediction of τ/σ in each experiment with one minor exception —the data point for 14 June 2016. In this case (28) with $\kappa = 0.9$ provides a slightly superior prediction (Figure 6). (Use of diverse values of κ in (28) shows that $\kappa = 0.9$ yields that equation's best overall predictions. The optimal value $\kappa = 0.9$ in (28) differs from the optimal value $\kappa = 0.7$ in (29) for several reasons, but most notably because the orientation of the surfaces on which lateral pressures exert force differs in the derivations of (28) and (29). For (28) these lateral surfaces are normal to the sloping bed, and for (29) they are vertical.)

Another important result illustrated in Figure 6 is that the infinite-slope approximation, equation (27), yields predictions of τ/σ that err by an average of 125%. The predictions are universally too large because equation (1) consistently underestimates values of σ and equation (2) consistently overestimates values of τ for cases in which a debris mass thickens in the downslope direction. In comparison, the prediction errors of (29) with $\kappa = 0.7$ average 11.0% percent, and the prediction errors of (28) with $\kappa = 0.9$ average 14.5%.

5.3. Apparent Basal Coulomb Friction With DEM Topography

Full engagement of Coulomb friction at the base of sloping debris masses is described by $|\tau/\sigma| = \tan\phi$ if the stress components τ and σ act directly on the sloping bed where friction acts. For this limiting equilibrium state, accurate measurements or calculations of τ and σ suffice to determine the value of the effective basal friction angle, ϕ, which implicitly accounts for any pore pressure effects. However, identification of a suitable basal friction angle is less straightforward if a slope is represented by discretized staircase topography, as it is in a DEM. In this case the applicable force balance describing a Coulomb limiting equilibrium state involves the stress components τ_{ZX} and σ_{ZZ} acting on the staircase treads, and the ratio $|\tau_{ZX}/\sigma_{ZZ}|$ serves as an appropriate measure of engaged basal friction. Employing (13) and (14) to evaluate this stress ratio yields

$$|\tau_{ZX}/\sigma_{ZZ}| = \kappa|\tan\beta| = \tan\phi_{\text{tread}}, \tag{30}$$

where ϕ_{tread} is the apparent basal friction angle on the horizontal treads of the staircase, and the absolute values of τ_{ZX}/σ_{ZZ} and $\tan\beta$ indicate that ϕ_{tread} must be nonnegative, even if τ_{ZX} and β are negative. There is little reason to expect that $\phi_{\text{tread}} = \phi$ would apply in (30) because the tread has an orientation and surface area that differ from those of the sloping surface on which friction physically acts. Nevertheless, ϕ_{tread} has clear importance because it is the apparent friction angle that is necessary to produce a balanced limiting equilibrium state if friction is assumed to act on the horizontal treads of a staircase rather than on a sloping bed.

Table 4
Summary of Equations Relating ϕ_{tread} to ϕ, θ, κ and β as Well as the Applicable Horizontal, Limit-Equilibrium Force Balance

Range of applicability	Equation relating ϕ_{tread} to ϕ, θ and κ	Equations governing horizontal, limit equilibrium force balance
$\beta \geq 0$	$\tan\phi_{tread} = \text{sgn}(\beta)[\kappa \tan\theta + \tan(\phi - \theta)]$	$\tan\phi_{tread} = \kappa \tan\beta$ $\kappa(\tan\beta - \tan\theta) = \tan(\phi - \theta)$
$\beta < 0$ and $\tan\beta \geq (1 - \frac{1}{\kappa})\tan\theta$	$\tan\phi_{tread} = \text{sgn}(\beta)[\kappa \tan\theta + \tan(\phi - \theta)]$	$\tan\phi_{tread} = -\kappa \tan\beta$ $\kappa(\tan\beta - \tan\theta) = \tan(\phi - \theta)$
$\beta < 0$ and $\tan\beta \leq (1 - \frac{1}{\kappa})\tan\theta$	$\tan\phi_{tread} = -\kappa \tan\theta + \tan(\phi + \theta)$	$\tan\phi_{tread} = -\kappa \tan\beta$ $\kappa(\tan\beta - \tan\theta) = -\tan(\phi + \theta)$

Note. All equations assume that $\theta \geq 0$ applies.

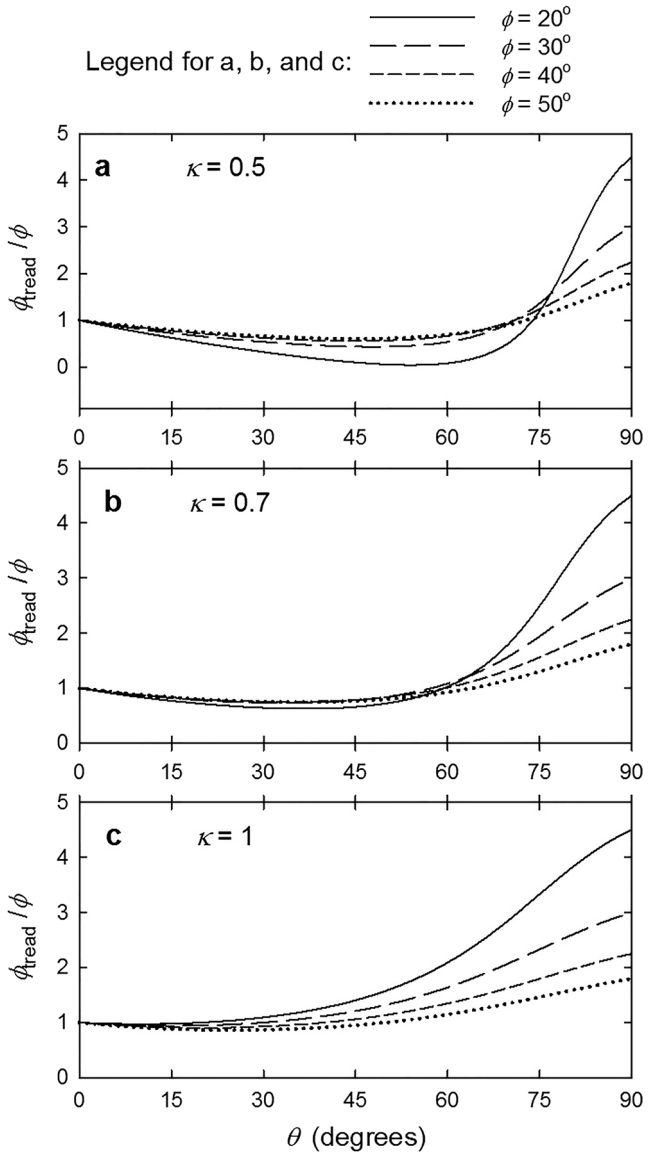

Figure 7. Graphs of solutions of equations (32) and (33), illustrating how ϕ_{tread}/ϕ varies as a function of the mean basal slope angle θ depicted in Figure 2. Graphs are shown for various plausible values of the basal friction angle ϕ and lateral pressure coefficient κ. All graphs assume that $\theta \geq 0$ applies and that either $\beta \geq 0$ or $\tan\beta > [1 - (1/\kappa)]\tan\theta$ applies. (a) $\kappa = 0.5$, (b) $\kappa = 0.7$, and (c) $\kappa = 1$.

Explicit relationships between ϕ_{tread} and ϕ can be obtained by exploiting the fact that both (29) and (30) describe a state of limiting equilibrium if $\tau/\sigma = \tan\phi$ and $H_\tau/H_\sigma = 1$ apply. This condition allows (29) and (30) to be treated as simultaneous equations. However, the resulting relationship between ϕ_{tread} and ϕ varies somewhat depending on the sign and value of β, because these properties determine the signs of the basal shear stresses τ and τ_{ZX} (Table 4). We focus first on the case illustrated in Figures 1 and 2, in which $\beta > 0$, $\tau > 0$, and $\tau_{ZX} > 0$ apply. For this case, (29) can be reduced to the form

$$\tan\phi = \frac{(1-\kappa)\tan\theta + \tan\phi_{tread}}{1 + \kappa\tan^2\theta - \tan\theta\tan\phi_{tread}}. \quad (31)$$

(This form is obtained from (29) by using (30) to replace $\kappa \tan\beta$ with $\tan\phi_{tread}$ and using the Coulomb limit equilibrium equation to replace τ/σ with $\tan\phi$.) Some algebraic manipulation of (31) followed by use of a well-known trigonometric identity (e.g., Dwight, 1961, equation 405.02) then yields

$$\tan\phi_{tread} = \kappa\tan\theta + \tan(\phi - \theta). \quad (32)$$

For slopes inclined at nearly the angle of repose, such that $\phi \approx \theta$ applies, (32) reduces to the approximation $\tan\phi_{tread} \approx \kappa \tan\theta \approx \kappa \tan\phi$. More generally, (32) indicates that applicable values of ϕ_{tread} can be either larger or smaller than those of ϕ, depending on the values of θ and κ.

The significance of (32) for slope stability computations that use discretized DEM topography can be illustrated by using the equation to graph ϕ_{tread}/ϕ as a function of θ for values of κ ranging from 0.5 to 1 and values of ϕ ranging from 20° to 50° (Figure 7). If $\kappa = 0.5$ applies, then values of ϕ_{tread}/ϕ are generally smaller than 1 unless a very steep basal slope with $\theta > 70°$ exists (Figure 7a). On the other hand, if $\kappa = 1$ applies, then values of ϕ_{tread}/ϕ exceed 1 for all cases in which $\theta > \phi$ applies, and in some cases the value of ϕ_{tread} exceeds that of ϕ by a factor of 2 or more (Figure 7c). Behavior that is intermediate between those with $\kappa = 0.5$ and $\kappa = 1$ is evident if $\kappa = 0.7$ applies (Figure 7b).

Equations that differ slightly from (32) apply for cases with adverse surface slopes (i.e., slopes with $\beta < 0$). If $\beta < 0$ and $\tan\beta > [1 - (1/\kappa)]\tan\theta$ each apply, then basal shear stresses on a smoothly sloping bed and staircase treads have opposite signs, such that $\tau > 0$ and $\tau_{XZ} < 0$ each apply. In this case a derivation that parallels the derivation of (32) yields the result $\tan\phi_{tread} = -[\kappa \tan\theta + \tan(\phi - \theta)]$. This result and (32) can be consolidated into a single equation expressed as

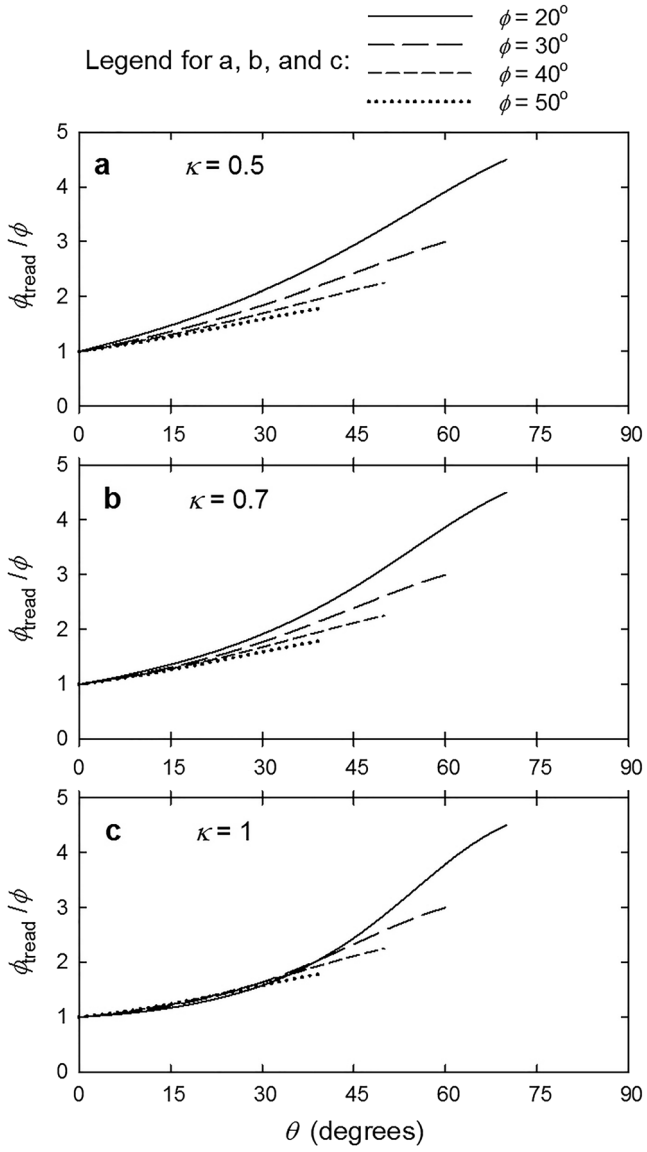

Figure 8. Graphs of solutions of equation (34), illustrating how ϕ_{tread}/ϕ varies as a function of the mean basal slope angle θ depicted in Figure 2. Graphs are shown for various plausible values of the basal friction angle ϕ and lateral pressure coefficient κ. All graphs assume that $\theta \geq 0$, $\beta < 0$, and $\tan\beta < [1 - (1/\kappa)] \tan\theta$ apply. (a) $\kappa = 0.5$, (b) $\kappa = 0.7$, and (c) $\kappa = 1$.

$$\tan\phi_{tread} = \text{sgn}(\beta)[\kappa \tan\theta + \tan(\phi - \theta)], \quad (33)$$

where sgn(β) denotes the sign of β (Table 4). This equation implies that $\tan\phi_{tread} \geq 0$ is always satisfied, because the sign of β is the same as that of $[\kappa \tan\theta + \tan(\phi - \theta)]$ for scenarios that satisfy a limiting equilibrium force balance (Table 4). Equation (33) additionally implies that the family of graphs portrayed in Figure 7 is also valid for cases with gentle adverse surface slopes if $\tan\beta > [1 - (1/\kappa)] \tan\theta$ applies.

If an adverse surface slope is steeper, such that $\tan\beta < [1 - (1/\kappa)] \tan\theta$ applies, then the basal shear stresses acting on a smoothly sloping bed and staircase treads are each negative (i.e., they act in the negative x and negative X directions of Figures 1 and 2). In this case a derivation that parallels the derivation of (32) yields

$$\tan\phi_{tread} = -\kappa \tan\theta + \tan(\phi + \theta). \quad (34)$$

Graphs of this equation are illustrated in Figure 8, and they differ from those in Figure 7. One of the most important differences is that they indicate that values of ϕ_{tread} universally exceed those of ϕ if $\theta > 0$ applies. Additionally, the graphs are truncated where $\phi + \theta \rightarrow 90^\circ$ occurs, because no limit equilibrium horizontal force balance is attainable if $\phi + \theta \geq 90^\circ$ applies, regardless of the values of β or κ.

The limit equilibrium horizontal force balance equations that accompany (33) and (34) differ from one another, as summarized in Table 4. They show that if $\beta = \theta$ applies (which requires that $\beta > 0$ applies), then a state of Coulomb limiting equilibrium requires that $\phi = \theta$ is satisfied, consistent with the behavior of an infinite slope. Another important special case is that in which $\beta = 0$ and $\kappa = 1$ apply, as is true for a static liquid. In this case the force balances show that a limiting equilibrium state exists only if $\phi = 0$ applies, regardless of the value of θ. The value $\phi = 0$ also applies to a limiting equilibrium force balance for the special case in which an adverse slope satisfies $\tan\beta = [1 - (1/\kappa)] \tan\theta$, regardless of the value of κ. Physically, this special case corresponds to one with zero basal shear stress on a smoothly sloping bed ($\tau = 0$) but finite basal shear stress on a staircase tread, and in this case the tread friction satisfies $\tan\phi_{tread} = (1 - \kappa) \tan\theta = -\kappa \tan\beta$.

6. Discussion

Unlike formulas derived from infinite-slope or shallow-debris assumptions, our new basal stress formulas place few restrictions on the angles that characterize the surface slope and basal slope of a debris mass. Our derivations of all formulas assume that the basal slope angle θ is positive, but the formulas are equally valid for cases with $\theta < 0$. For such cases, the formulas involve mirror images of the angles θ and β illustrated in Figures 1 and 2. Thus, a case with $\theta > 0$ and $\beta < 0$ is exactly analogous to a case with $\theta < 0$ and $\beta > 0$ because it is a mirror image of that case.

The approach we use to obtain our new basal stress formulas has similarities to approaches employed in some methods of slices or columns used in classical slope stability analyses (e.g., Bromhead, 1986). However, to our knowledge our approach does not duplicate any of these approaches. It can nevertheless be employed much as methods of slices are employed—by aligning adjacent slices or columns with various bed slopes and surface slopes and then summing a series of local forces to obtain a global force balance for the assemblage. In such an application, our formulas imply that lateral forces acting on the vertical faces of adjacent columns balance one another, but one column nevertheless exerts additional force on an adjacent

column downslope if its basal friction is too small to support its calculated τ/σ value. In this case the compressional action-reaction force pair acting on the shared vertical faces of the adjacent columns must increase, implying that the applicable local value of the lateral pressure coefficient κ must be larger than an "at rest" value such as that calibrated in our experiments.

Our new basal stress formulas also can be applied in depth-averaged dynamic models such as those of Savage and Hutter (1989) and Iverson and George (2014). When employed in this way, the formulas can be used to identify areas of local instability in static source areas. Onset of subtle motion at these locations may subsequently lead to more widespread motion through the process of momentum exchange—contingent on whether material in adjacent computational cells has sufficient basal frictional resistance to counteract the momentum influx (e.g., Iverson & George, 2016). Again, in such scenarios, with regions of both compressional and extensional deformation, applicable values of κ may vary and differ from the value calibrated in our experiments (cf. Hungr, 2008).

Our results concerning the apparent basal Coulomb friction that applies if topography is represented by a staircase function have large implications for both slope stability analyses and depth-averaged debris dynamics analyses that employ unsmoothed discretized base topography as represented in DEMs. The requisite adjustment of basal friction might be viewed as an artifact associated with use of DEM staircase topography, but it is nevertheless essential to ensure accurate force balances in such models. We are unaware of any prior study that has identified this requirement.

Application of our staircase basal friction formulas in dynamic models involves some subtleties that are beyond the scope of this paper, however. Whereas the direction of action of the frictional resisting force for a static debris mass is relatively straightforward (because basal frictional resistance must oppose and balance the net static driving force), frictional resistance opposes motion—not net forcing—of a moving debris mass irrespective of its geometry. Thus, the simple geometric criteria established in this paper for evaluating the direction and magnitude of the apparent frictional force may need to be generalized for application in dynamic models. Computations and experiments that involve rapid changes in the direction of motion during multidimensional flow interactions with adverse slopes and topographic barriers provide good test cases for such generalizations (e.g., Iverson et al., 2016).

7. Conclusions

The findings we report here support the following conclusions:

1. Newly derived algebraic formulas provide estimates of basal normal stress and shear stress that on average err by less than 3% and 13%, respectively, in predicting basal stresses measured in six large-scale experiments involving steeply sloping, wet debris masses with varying geometries and compositions. For the conditions investigated in these experiments, much larger prediction errors result from use of infinite-slope or shallow-debris approximations.
2. The derivations of the new basal stress formulas place few restrictions on the ranges of surface slope angles or basal slope angles for which they apply.
3. The new basal stress formulas include a single tuning parameter, a lateral pressure coefficient κ, but a fixed value $\kappa = 0.7$ yields good predictions for the full range of conditions investigated in our experiments.
4. Specialized versions of the basal stress formulas apply if smoothly sloping terrain is discretized and represented by a staircase function, as it is in DEMs.
5. If basal terrain is represented by a staircase function, then accurate evaluation of limiting equilibrium conditions in which Coulomb friction is engaged on the horizontal surfaces (or treads) of the staircase requires an adjustment of the apparent basal Coulomb friction angle. For most debris masses, including all debris masses with nonnegative surface slopes ($\beta \geq 0$), the adjustment can be expressed as $\tan\phi_{\text{tread}} = \text{sgn}(\beta)[\kappa \tan\theta + \tan(\phi - \theta)]$, where θ is the local staircase slope angle, ϕ_{tread} is the apparent Coulomb friction angle of debris contacting the treads of the staircase, and ϕ is the true basal friction angle of the same debris in contact with a bed sloping smoothly at the angle θ. For debris masses with adverse surface slopes that are steep enough to satisfy $\tan\beta < [1 - (1/\kappa)] \tan\theta$, the adjustment is expressed as $\tan\phi_{\text{tread}} = -\kappa \tan\theta + \tan(\phi + \theta)$.
6. Slope-dependent differences between the values of ϕ_{tread} and ϕ may demand modifications or corrections of numerical simulations that employ staircase basal topography as represented in DEMs.

Appendix A: Derivation of Equation (3)

A brief derivation of equation (3) is provided here to clarify the equation's origin and physical basis. The derivation begins by employing the Cauchy momentum-conservation equation, which expresses Newton's second law of motion as it applies to continuum mechanics (e.g., *Malvern*, 1969). For a continuous body of debris in contact with a bed sloping at an angle θ on Earth's surface, the x (downslope) component of the Cauchy equation may be expressed as

$$\rho\frac{\mathrm{d}u}{\mathrm{d}t} = \rho g\sin\theta - \frac{\partial\sigma_{xx}}{\partial x} + \frac{\partial\tau_{yx}}{\partial y} + \frac{\partial\tau_{zx}}{\partial z}. \tag{A1}$$

Here u is the downslope component of velocity and $\mathrm{d}/\mathrm{d}t$ is a material total time derivative defined as $\mathrm{d}/\mathrm{d}t = \partial/\partial t + u(\partial/\partial x) + v(\partial/\partial y) + w(\partial/\partial z)$, where v and w are the cross-slope (y) and slope-normal (z) components of velocity, respectively. Terms on the right-hand side of (A1) express the effects of a driving force due to the downslope component of Earth's gravitational acceleration, $g\sin\theta$, and of resisting forces due to spatial gradients in the stress components σ_{xx}, τ_{yx}, and τ_{zx}. The sign of the slope-parallel normal stress σ_{xx} differs from the signs of the slope-parallel shear stresses τ_{yx} and τ_{zx} because we define σ_{xx} using a geomechanics sign convention in which compression is positive but define τ_{yx} and τ_{zx} using a standard continuum mechanics sign convention.

The first step in our reduction of (A1) involves depth integration of the equation from the base of the debris mass at $z = z_{\mathrm{bed}}$ to its stress-free upper surface at $z = h$. Mathematical details of the integration are somewhat cumbersome but are presented in detail by Iverson and Ouyang (2015). The result of the integration can be expressed as

$$\overline{\rho}h\frac{\overline{\mathrm{d}}\overline{u}}{\overline{\mathrm{d}}t} = \overline{\rho}gh\sin\theta - \frac{\partial(\overline{\sigma}_{xx}h)}{\partial x} - \tau_{xx\ \mathrm{bed}}\frac{\partial z_{\mathrm{bed}}}{\partial x} + \frac{\partial(\overline{\tau}_{yx}h)}{\partial y} + \tau_{yx\ \mathrm{bed}}\frac{\partial z_{\mathrm{bed}}}{\partial y} - \tau_{zx\ \mathrm{bed}}, \tag{A2}$$

where overbars denote depth-averaged quantities, and the depth-averaged material time derivative is defined as $\overline{\mathrm{d}}/\overline{\mathrm{d}}t = \partial/\partial t + \overline{v}(\partial/\partial y) + \overline{w}(\partial/\partial z)$. The left-hand side of (A2) is an approximation insofar as it neglects the effects of differential advection of momentum due to variations of velocity or bulk density with depth. By contrast, the right-hand side of (A2) is exact. It involves no assumptions about rheology that might influence the various stress components, including the basal shear stress $\tau_{zx\ \mathrm{bed}}$.

The next steps in our derivation assume that steady state mechanical equilibrium exists (i.e., $\overline{\mathrm{d}}\overline{u}/\overline{\mathrm{d}}t = 0$), that effects of stress variations in the cross-slope direction can be neglected (i.e., $\partial(\overline{\tau}_{yx}h)/\partial y = 0$), and that the origin of the z coordinate lies on the plane of the bed (i.e., $z_{\mathrm{bed}} = 0$). In this case (A2) reduces to a simple expression for the basal shear stress,

$$\tau_{zx\ \mathrm{bed}} = \overline{\rho}gh\sin\theta - \frac{\partial(\overline{\sigma}_{xx}h)}{\partial x}. \tag{A3}$$

Use of (A3) to obtain equation (3) of the main text involves two key physical assumptions. The first is that the normal stress acting on planes parallel to the bed, σ_{zz}, is the geostatic normal stress given by

$$\sigma_{zz} = \rho g\cos\theta(h - z). \tag{A4}$$

This assumption is widely applied in analyses of geophysical problems, but it is strictly valid only if $\partial h/\partial x = 0$ applies. In other words, it is valid only for one-dimensional stress states like those assumed in the derivations of equations (1) and (2) in the main text. Equation (A4) also assumes that no acceleration occurs normal to the bed, but this assumption can be relaxed by modifying the effective value of g.

The second key assumption is that the slope-parallel normal stress, σ_{xx}, is proportional to σ_{zz}, such that

$$\sigma_{xx} = \kappa\sigma_{zz} = \kappa\rho g\cos\theta(h - z) \tag{A5}$$

applies, where κ is a proportionality coefficient. This assumption is also widely applied in geophysical analyses, and in various contexts κ can be interpreted as an elastic constant, a fluid constant (typically κ=1), or a

Rankine or Coulomb earth-pressure coefficient (which has different values for compressional or extensional plastic equilibrium states). Here we treat κ simply as a tuning parameter. Consequently, the use of κ in (A5) entails an assumption that is less fundamental than the use of (A4) to obtain (A5).

The final step in deriving equation (3) of the main text begins with depth integration of (A5), which yields an expression for the depth-averaged longitudinal normal stress

$$\overline{\sigma}_{xx} = \frac{1}{h}\int_0^h \kappa\rho g \cos\theta (h-z)\mathrm{d}z = \frac{1}{2}\kappa\bar{\rho}gh\cos\theta. \tag{A6}$$

Substitution of (A6) into (A3) then yields

$$\tau_{zx\ \mathrm{bed}} = \bar{\rho}gh\sin\theta - \kappa\bar{\rho}gh\cos\theta\frac{\partial h}{\partial x}, \tag{A7}$$

which matches equation (3) of the main text, albeit with minor differences in notation.

Appendix B: Moment Limit Equilibrium

Our analysis of moment limiting equilibrium considers a quadrilateral body with a geometry similar to that of the shaded body illustrated in Figure 1 but with a different origin of coordinates. The analysis identifies states in which the body is poised to undergo rigid-body rotation that causes it to topple in the downslope direction. It applies for all values of β and θ, but it emphasizes cases in which $\beta > 0$ and $\theta > 0$ apply. If $\beta > \theta$ also applies, then the upper surface of the body slopes more steeply than its basal surface, enhancing the potential for the body to topple.

We evaluate moment equilibrium by analyzing torques that act through a pivot point located at the lowest corner of the body, where we define an origin of rectangular Cartesian coordinates as $(X,Z) = (0,0)$. We use H_1 to denote the height of the downslope lateral boundary of the body, which rises vertically from the origin, and we use H_2 to denote the height of the upslope lateral boundary of the body. The elevation of the basal boundary of the body is described by $b(X) = X\tan\theta$, and the elevation of the upper surface of the body is described by $\eta(X) = H_1 + X\tan\beta$. The body extends horizontally from $X = 0$ to $X = L$, and the cross-slope breadth of the body is B. Therefore, the mass M and weight W of the body are described by

$$M = \rho LB\frac{H_1 + H_2}{2}, \qquad W = Mg. \tag{B1, B2}$$

The weight W acts vertically, and it is one of three forces that influence moment equilibrium. The other two forces are the horizontally acting lateral pressure forces described by

$$F_1 = \frac{1}{2}\kappa\rho gB{H_1}^2, \qquad F_2 = -\frac{1}{2}\kappa\rho gB{H_2}^2. \tag{B3, B4}$$

The crux of the moment analysis involves finding the moment arms through which the forces F_1, F_2, and W exert torques that act to rotate the body about the pivot point $(X,Z) = (0,0)$.

Finding the moment arm for F_1 is simple because this force acts at the centroid of a lateral pressure distribution in which the pressure is assumed to increase linearly with depth. Elementary analytical geometry shows that the centroid of this pressure distribution is located at the elevation $Z = (1/3)H_1$. Thus, the moment arm is $H_1/3$, implying that the moment due to F_1 is given by

$$m_1 = \frac{1}{3}H_1F_1 = \frac{1}{6}\kappa\rho gB{H_1}^3. \tag{B5}$$

Finding the moment due to F_2 is no different in principle from finding m_1, but it is a more complicated procedure because the centroid of the linear lateral pressure distribution that produces F_2 is located at an elevation $Z = L\tan\theta + (1/3)H_2$. Furthermore, because we aim to eliminate H_2 from our results, we express H_2 as $H_2 = H_1 + L(\tan\beta - \tan\theta)$, so that the moment arm for F_2 becomes $L\tan\theta + (1/3)$

$[H_1+L(\tan\beta - \tan\theta)]$. Multiplying this moment arm with (B4) and algebraically manipulating the resulting expression yields the moment due to F_2:

$$m_2 = -\frac{1}{6}\,\kappa\,\rho g B\left[{H_1}^3 + 3{H_1}^2 L\tan\beta + 3H_1L^2\left(\tan^2\beta - \tan^2\theta\right) + L^3\left(\tan^3\beta + 2\tan^3\theta - 3\tan^2\theta\tan\beta\right)\right] \quad \text{(B6)}$$

The moment arm for the weight force W is given by the X coordinate of the center of mass of the body, X_{CM}. This coordinate is found by integrating the product of X and the mass distribution of the body throughout its extent in the X-Z plane:

$$X_{CM} = \frac{\rho B}{M}\int_0^L X \int_{X\tan\theta}^{H_1+X\tan\beta} \mathrm{d}Z\mathrm{d}X. \quad \text{(B7)}$$

Evaluating the integrals in (B7) and combining the result with (B1) enables elimination of $\rho B/M$ and yields

$$X_{CM} = \frac{H_1L + \frac{2}{3}L^2(\tan\beta - \tan\theta)}{H_1 + H_2}. \quad \text{(B8)}$$

This equation simplifies further because the geometry of the body indicates that the relationship $\tan\beta - \tan\theta = (H_2 - H_1)/L$ applies. Substituting this relationship in (B8) and manipulating the algebra then reduces (B8) to

$$X_{CM} = L\frac{H_1 + 2H_2}{3(H_1 + H_2)}. \quad \text{(B9)}$$

Finally, the moment $m_3 = WX_{CM}$ due to the weight force W is found by using (B1) and (B2) in conjunction with (B9) and the substitution $H_2 = H_1+L(\tan\beta - \tan\theta)$ to obtain

$$m_3 = \frac{1}{2}\rho g B L^2\left[H_1 + \frac{2}{3}L(\tan\beta - \tan\theta)\right]. \quad \text{(B10)}$$

The last step in calculating the moment equilibrium of the body entails adding (B5), (B6), and (B10) to find the total moment $m = m_1+m_2+m_3$, setting $m = 0$, and manipulating the equation $m = 0$ algebraically to obtain a dimensionless quadratic equation:

$$\left[\kappa\left(\frac{1}{3}\tan^3\beta + \frac{2}{3}\tan^3\theta - \tan^2\theta\tan\beta\right) - \frac{2}{3}(\tan\beta - \tan\theta)\right]\left(\frac{L}{H_1}\right)^2 + \left[\kappa(\tan^2\beta - \tan^2\theta) - 1\right]\left(\frac{L}{H_1}\right) + \kappa\tan\beta = 0. \quad \text{(B11)}$$

For the special case of an infinite slope, in which $\beta = \theta$ applies, the dimensionless moment balance (B11) reduces to

$$L/H_1 = \kappa\tan\beta. \quad \text{(B12)}$$

Thus, for increasingly steep surface slopes and lateral pressures, which are indicated by larger values of $\kappa\tan\beta$, an increasingly large length-to-thickness ratio of the body, L/H_1, is necessary in order to maintain moment equilibrium. On the other hand, if $\beta = 0$ applies, then moment equilibrium can be satisfied only in the limit of a vanishingly slender body, with $L/H_1 \to 0$.

Similar principles apply to the moment limit equilibrium of quadrilateral bodies of nonuniform thickness, but solutions of (B11) indicate that the geometric influence of the body shape in these cases can be quite complex. Graphs of such solutions for cases with $\kappa = 1$ are illustrated in Figure B1, in which increasing values of L/H_1 imply an increasing propensity for toppling (i.e., they imply that relatively short, squat body geometries are necessary to prevent failure by toppling). The curves in Figure B1 show that the moment

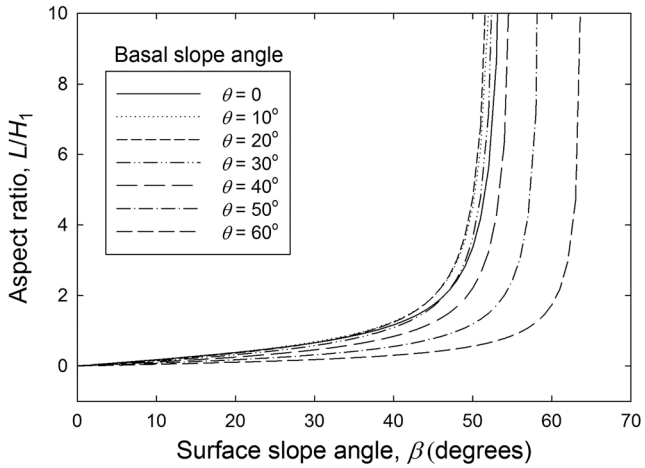

Figure B1. Graphs of solutions of equation (B11) for cases with $\kappa = 1$, illustrating conditions of limiting moment equilibrium that apply when a laterally bounded quadrilateral body is on the verge of toppling in the downslope direction. L is the horizontal length of the body, and H_1 is the vertical height of the downslope margin of the body.

equilibrium is sensitive to the surface slope angle, particularly for $\beta > 40^\circ$. Indeed, for very steep surface slopes, with $\beta > 60^\circ$, moment equilibrium is nearly impossible to attain because it additionally requires a very steep basal slope, with $\theta > 50^\circ$. (The fact that moment equilibrium can be enhanced by increasing the angle of the basal slope may seem counterintuitive, but it is a consequence of the reduction of the downslope lateral force that occurs in conjunction with raising the bed elevation beneath the upslope boundary of the quadrilateral.) On the other hand, Figure B1 also shows that the moment limit equilibrium of quadrilaterals with basal slope angles that satisfy $\theta \leq 30^\circ$ differs little from that of quadrilaterals resting on flat basal surfaces ($\theta = 0$).

Acknowledgments
We thank the many colleagues who participated in the USGS debris flow flume experiments conducted in June 2016: Matthew Logan, Chris Lockett, Kelly Swinford, Kate Allstadt, Maxime Farin, Doug Tebo, Joel Smith, Jason Kean, Andy Lockhart, Luke McGuire, Francis Rengers, Aaron Rhinehart, and Victor Tsai. We also thank Rex Baum, Mark Reid, Christophe Ancey, John Buffington, and two anonymous referees for useful comments on our manuscript. All data utilized in this manuscript can be freely downloaded from the USGS ScienceBase archive at the website (https://doi.org/10.5066/F7N58JKH). Any use of trade, firm, or product names in this publication is for descriptive purposes only and does not imply endorsement by the U.S. Government.

References

Bouchut, F., Mangeney-Castelnau, A., Perthame, B., & Vilotte, J.-P. (2003). A new model of Saint Venant and Savage–Hutter type for gravity driven shallow water flows. *Comptes Rendus Mathematique*, *336*(6), 531–536. https://doi.org/10.1016/S1631-073X(03)00117-1

Bromhead, E. N. (1986). *The stability of slopes*. London: Surrey University Press.

Dwight, H. B. (1961). *Tables of integrals and other mathematical data* (4th ed.). New York: MacMillan.

Fang, Y.-S., Chen, J.-M., & Chen, C.-Y. (1997). Earth pressures with sloping backfill. *Journal of Geotechnical and Geoenvironmental Engineering*, *123*(3), 250–259. https://doi.org/10.1061/(ASCE)1090-0241(1997)123:3(250)

George, D. L., Iverson, R. M., & Cannon, C. M. (2017). New methodology for computing tsunami generation by subaerial landslides: application to the 2015 Tyndall Glacier Landslide, Alaska. *Geophysical Research Letters*, *44*, 7276–7284. https://doi.org/10.1002/2017GL074341

Hungr, O. (2008). Simplified models of spreading flow of dry granular material. *Canadian Geotechnical Journal*, *45*(8), 1156–1168. https://doi.org/10.1139/T08-059

Iverson, R. M. (1997). The physics of debris flows. *Reviews of Geophysics*, *35*(3), 245–296. https://doi.org/10.1029/97RG00426

Iverson, R. M., & Denlinger, R. P. (2001). Flow of variably fluidized granular masses across three-dimensional terrain: 1. Coulomb mixture theory. *Journal of Geophysical Research*, *106*(B1), 537–552. https://doi.org/10.1029/2000JB900329

Iverson, R. M., & George, D. L. (2014). A depth-averaged debris-flow model that includes the effects of evolving dilatancy. I. physical basis. *Proceedings of the Royal Society A: Mathematical, Physical and Engineering Sciences*, *470*(2170). https://doi.org/10.1098/rspa.2013.0819

Iverson, R. M., & George, D. L. (2016). Modeling landslide liquefaction, mobility bifurcation, and the dynamics of the 2014 Oso disaster. *Géotechnique*, *66*(3), 175–187. https://doi.org/10.1680/jgeot.15.LM.004

Iverson, R. M., George, D. L., & Logan, M. (2016). Debris flow runup on vertical barriers and adverse slopes. *Journal of Geophysical Research: Earth Surface*, *121*, 2333–2357. https://doi.org/10.1002/2016JF003933

Iverson, R. M., & Logan M. (2017). Sensor data from debris-flow experiments conducted in June, 2016, at the USGS debris-flow flume, HJ Andrews Experimental Forest, Blue River, Oregon: U.S. Geological Survey data release. https://doi.org/10.5066/F7N58JKH.

Iverson, R. M., Logan, M., LaHusen, R. G., & Berti, M. (2010). The perfect debris flow? Aggregated results from 28 large-scale experiments. *Journal of Geophysical Research*, *115*, F03005. https://doi.org/10.1029/2009JF001514

Iverson, R. M., & Ouyang, C. (2015). Entrainment of bed material by Earth-surface mass flows: review and reformulation of depth-integrated theory. *Reviews of Geophysics*, *53*, 27–58. https://doi.org/10.1002/2013RG000447

Keller, J. B. (2003). Shallow-water theory for arbitrary slopes of the bottom. *Journal of Fluid Mechanics*, *489*, 345–348. https://doi.org/10.1017/S0022112003005342

Lade, P. V., & De Boer, R. (1997). The concept of effective stress for soil, concrete and rock. *Géotechnique*, *47*(1), 61–78. https://doi.org/10.1680/geot.1997.47.1.61

LeVeque, R. J., George, D. L., & Berger, M. J. (2011). Tsunami modelling with adaptively refined finite volume methods. *Acta Numerica*, 211–289. https://doi.org/10.1017/S0962492911000043

Major, J. J., & Iverson, R. M. (1999). Debris-flow deposition—Effects of pore-fluid pressure and friction concentrated at flow margins. *Geological Society of America Bulletin*, *111*(10), 1424–1434. https://doi.org/10.1130/0016-7606(1999)111<1424:DFDEOP>2.3.CO;2

Malvern, L. E. (1969). *Introduction to the mechanics of a continuous medium*. Englewood Cliffs: Prentice-Hall.

Savage, S. B., & Hutter, K. (1989). The motion of a finite mass of granular material down a rough incline. *Journal of Fluid Mechanics*, *199*(1), 177–215. https://doi.org/10.1017/S0022112089000340

Savage, S. B., & Hutter, K. (1991). The dynamics of avalanches of granular materials from initiation to runout. Part I: Analysis. *Acta Mechanica*, *86*(1-4), 201–223. https://doi.org/10.1007/BF01175958